



## RESEARCH ARTICLE

10.1029/2018JD029619

## Evidence of Isotopic Fractionation During Vapor Exchange Between the Atmosphere and the Snow Surface in Greenland

## Key Points:

- Data show evidence of isotopic fractionation during vapor exchange between the snow surface and atmosphere
- Model simulations suggest diurnal variation in the snow surface isotopic composition
- We propose an enhanced effective isotopic exchange between the surface of the snow grain and its interior

## Supporting Information:

- Supporting Information S1
- Data Set S1
- Data Set S2
- Data Set S3
- Data Set S4
- Data Set S5
- Data Set S6
- Data Set S7
- Data Set S8

## Correspondence to:

H. C. Steen-Larsen,  
hans.christian.steen-larsen@uib.no

## Citation:

Madsen, M. V., Steen-Larsen, H. C., Hörhold, M., Box, J., Berben, S. M. P., Capron, E., et al. (2019). Evidence of isotopic fractionation during vapor exchange between the atmosphere and the snow surface in Greenland. *Journal of Geophysical Research: Atmospheres*, 124, 2932–2945. <https://doi.org/10.1029/2018JD029619>

Received 6 SEP 2018

Accepted 9 FEB 2019

Accepted article online 18 FEB 2019

Published online 18 MAR 2019

M. V. Madsen<sup>1</sup> , H. C. Steen-Larsen<sup>1,2</sup> , M. Hörhold<sup>3</sup> , J. Box<sup>4</sup> , S. M. P. Berben<sup>5</sup> , E. Capron<sup>1,6</sup> , A.-K. Faber<sup>2,5</sup> , A. Hubbard<sup>7,8</sup> , M. F. Jensen<sup>5</sup> , T. R. Jones<sup>9</sup> , S. Kipfstuhl<sup>3</sup> , I. Koldtoft<sup>1</sup> , H. R. Pillar<sup>10</sup> , B. H. Vaughn<sup>9</sup> , D. Vladimirova<sup>1</sup> , and D. Dahl-Jensen<sup>1,11</sup>

<sup>1</sup>Centre for Ice and Climate, University of Copenhagen, Copenhagen, Denmark, <sup>2</sup>Geophysical Institute and Bjerknes Centre for Climate Research, University of Bergen, Bergen, Norway, <sup>3</sup>Alfred-Wegener-Institute, Bremerhaven, Germany, <sup>4</sup>GEUS, Copenhagen, Denmark, <sup>5</sup>Department of Earth Science, University of Bergen and Bjerknes Centre for Climate Research, Bergen, Norway, <sup>6</sup>British Antarctic Survey, Cambridge, UK, <sup>7</sup>Centre for Glaciology, Department of Geography and Earth Sciences, Aberystwyth University, Aberystwyth, UK, <sup>8</sup>Centre for Arctic Gas Hydrate, Environment and Climate, Department of Geology, UiT-The Arctic University of Norway, Tromsø, Norway, <sup>9</sup>INSTAAR, University of Colorado Boulder, Boulder, CO, USA, <sup>10</sup>Oden Institute for Computational Engineering and Sciences, University of Texas at Austin, Austin, TX, USA, <sup>11</sup>Centre for Earth Observation Science, University of Manitoba, Winnipeg, Manitoba, Canada

**Abstract** Several recent studies from both Greenland and Antarctica have reported significant changes in the water isotopic composition of near-surface snow between precipitation events. These changes have been linked to isotopic exchange with atmospheric water vapor and sublimation-induced fractionation, but the processes are poorly constrained by observations. Understanding and quantifying these processes are crucial to both the interpretation of ice core climate proxies and the formulation of isotope-enabled general circulation models. Here, we present continuous measurements of the water isotopic composition in surface snow and atmospheric vapor together with near-surface atmospheric turbulence and snow-air latent and sensible heat fluxes, obtained at the East Greenland Ice-Core Project drilling site in summer 2016. For two 4-day-long time periods, significant diurnal variations in atmospheric water isotopologues are observed. A model is developed to explore the impact of this variability on the surface snow isotopic composition. Our model suggests that the snow isotopic composition in the upper subcentimeter of the snow exhibits a diurnal variation with amplitudes in  $\delta^{18}\text{O}$  and  $\delta\text{D}$  of  $\sim 2.5\text{‰}$  and  $\sim 13\text{‰}$ , respectively. As comparison, such changes correspond to 10–20% of the magnitude of seasonal changes in interior Greenland snow pack isotopes and of the change across a glacial-interglacial transition. Importantly, our observation and model results suggest, that sublimation-induced fractionation needs to be included in simulations of exchanges between the vapor and the snow surface on diurnal timescales during summer cloud-free conditions in northeast Greenland.

## 1. Introduction

Climate reconstructions derived from both Antarctic and Greenland ice cores constitute a cornerstone in paleoclimate science (e.g., Johnsen et al., 2001; Jouzel et al., 2007; Masson-Delmotte et al., 2015; Vimeux et al., 1999), extending to 129 thousand years (kyr) before present (BP; before 1950) in Greenland (North Greenland Ice-Core Project Members, 2004; NEEM Community Members, 2013), and to 800 kyr BP in Antarctica (EPICA Community Members, 2006; Jouzel et al., 2007). Interpretations of past climate variability using ice core water isotopes were determined using precipitation-weighted isotopic composition and observations of mean annual temperature either from in situ observations (e.g., Dansgaard, 1964; Johnsen et al., 2001; Jouzel et al., 1997), borehole temperature reconstruction (e.g., Vinther et al., 2010), or from use of distillation models (e.g., Johnsen et al., 1989; Masson-Delmotte et al., 2005; Uemura et al., 2012). These previous studies commonly assume that postdepositional processes do not influence the mean annual isotopic signature.

Recent advances in laser spectroscopy allow for field measurements of water isotopologue exchange between the snow surface and the atmosphere overlying the ice sheets. Steen-Larsen et al. (2014) reported concurrent isotopic variations in near-surface snow and atmospheric vapor at the North Greenland Eemian Ice Drilling (NEEM) camp, northwest Greenland. Over several precipitation-free periods (3–7 days), the surface (top

©2019. The Authors.

This is an open access article under the terms of the Creative Commons Attribution-NonCommercial-NoDerivs License, which permits use and distribution in any medium, provided the original work is properly cited, the use is non-commercial and no modifications or adaptations are made.

5 mm) snow  $\delta^{18}\text{O}$  varied by up to 6‰, attributable to vapor-exchange between the surface snow and atmospheric vapor. Ritter et al. (2016) deployed a laser spectrometer for measuring water vapor isotopes at Kohnen Station, East Antarctica. They showed that both surface snow and near-surface water vapor exhibit significant concurrent diurnal variations in water isotopic composition.

In a study by Casado et al. (2018), the authors combine a comprehensive dataset consisting of several years of precipitation collection from Dome C, Antarctica with  $\delta^{18}\text{O}$  records from snow pits. A clear discrepancy between the average precipitation isotopic composition and the average snow pit isotopic composition was observed. This demonstrated that the climate signal initially stored in the precipitation is not necessarily stored in the surface snow and subsequently buried, suggesting that the water isotopic composition of ice cores is not solely governed by precipitation. These studies highlight that isotopic exchange between atmospheric vapor and surface snow must be considered to accurately interpret observed variations in snow isotopic composition.

These previous observations of postdepositional change challenge the current parameterization of snow-air isotope exchange in isotope-enabled global circulation models, which are based on the assumption that sublimation does not change the surface snow isotopic composition (Risi et al., 2010; Werner et al., 2011; Wong et al., 2017). To link simulations using isotope-enabled global circulation models with ice core isotope records, it is therefore important to understand, quantify, and model the impact of postdepositional processes.

Here, we examine processes that control diurnal variations in snow and vapor isotopic composition in Greenland as a case study for the processes at play during sublimation and condensation. We pursue the hypothesis that snow and vapor isotopic composition is controlled through surface fluxes of water by both sublimation and deposition. To test our hypothesis we combine measurements of the isotopic composition of surface snow and near-surface atmospheric water vapor with estimates of atmospheric boundary layer (ABL) turbulence. To quantify the impact of postdepositional processes we advance upon previous studies and use a one-dimensional model to simulate our observed vertical profiles of atmospheric water vapor mixing ratio and isotopic composition above the snow surface, and the accompanying change in the isotopic composition of the surface snow. Our aim is to show that fluxes of water vapor between the snow surface and the atmosphere have the potential to change the snow isotopic composition. We acknowledge here that other relevant processes controlling the snow-air isotope exchange are neglected in this study. Development of a fully coupled atmosphere-snow boundary layer model with enabled isotopes is beyond the scope of the present study, but is an important direction for future research.

The paper is organized as follows. In section 2, we describe our observational methodology, reviewing the measurement site, characteristic meteorology, and instrumental configuration, along with the data acquisition, calibration, and the time series of observed variations in near-surface atmospheric humidity and water isotopologues. In section 3, we describe our near-surface atmospheric model. The model results are discussed in section 4, followed by conclusions and recommendations for further work in section 5.

## 2. Site Description and Methods

### 2.1. EastGRIP Site Location and Meteorological Characteristics

Sampling and measurements were conducted as part of the international deep ice core drilling project East Greenland Ice-Core Project (EastGRIP) from April to August 2016. The campsite was located in the northeast Greenland ice stream (75.63°N, 35.99°W; 2,700 m above sea level).

Meteorological observations were obtained from the Program for the Monitoring of the Greenland Ice Sheet (Ahlstrøm et al., 2008) using an automatic weather station (AWS), which was installed ~500 m southeast of the EastGRIP camp in May 2016. The summer 2016 (June-July-August) meteorological observations reported by the AWS are summarized in Table 1. The prevailing wind at the camp was westerly (Figure 1d). The surface air temperature (~2.5 m above the surface) varied between  $-35.0$  and  $-2.1$  °C, with a mean of  $-15.8$  °C.

During the measurement period (beginning of May to beginning of August), six precipitation events, corresponding to a total of 9 cm of snowfall, were recorded. The accumulation was estimated from measurements of snow heights along an array of 200 small bamboo sticks (1-cm diameter) deployed at the beginning of the season.

**Table 1**  
Summer 2016 (JJA) Minimum, Average, and Maximum Meteorological Values Reported by the PROMICE Automatic Weather Station at EastGRIP

	Minimum	Average	Maximum
Ambient air pressure	708 hPa	727 hPa	740 hPa
Wind speed	0.01 m/s	4.7 m/s	12.4 m/s
Air temperature	-35.0 °C	-15.8 °C	-2.1 °C
Relative humidity with respect to ice	54.6%	92.7%	113.7%

Note. JJA = June-July-August; EastGRIP = East Greenland Ice-Core Project; PROMICE = Programme for Monitoring of the Greenland Ice Sheet.

## 2.2. Cavity Ring-Down Spectrometry Measurements on Water Vapor and Surface Snow

During the 2016 field season, water stable isotopologues ( $^1\text{H}_2^{16}\text{O}$ ,  $^1\text{H}^2\text{H}^{16}\text{O}$ , and  $^1\text{H}_2^{18}\text{O}$ ) in near-surface vapor were measured continuously from 14 June to 4 August. The vapor measurement site (Figure 1) was located to the southwest (i.e., upwind) of camp at the edge of the clean air sector. Vapor samples were collected from four inlets mounted on a tower at initial heights of 0.52, 1.06, 2.07, and 7.20 m above the snow surface (Figure 1). For the rest of this study, these inlet heights are approximated as  $z = 0.5, 1, 2,$  and  $7$  m, respectively. No significant amount of accumulation occurred around the tower during the water vapor isotope measurement campaign. The tower consisted of an open aluminum frame

with a triangular footprint of  $\sim 20$ -cm-wide sides. The air was sampled through the inlets using a 10-L/min KNF pump (N811 KN.18) and measured using a Picarro L-2130 cavity ring-down spectrometer (CRDS). The CRDS was housed in a small heated tent (Figure 1), erected  $\sim 10$  m downwind from the tower. The full sampling protocol is described in Steen-Larsen et al. (2013), including regulation of both the vapor intake and analysis apparatus, which was done using solenoid valves measuring 15 min at each level.

Isotopic composition is reported using the notation  $\delta^* = (R^*/R^*_{\text{VSMOW}} - 1) \cdot 1,000\text{‰}$ , where  $R^*$  is the concentration ratio of the heavier isotopic species (with \* denoting either  $^1\text{H}^2\text{H}^{16}\text{O}$  or  $^1\text{H}_2^{18}\text{O}$ ) to the light abundant species ( $^1\text{H}_2^{16}\text{O}$ ) of water (Craig, 1961).  $R^*_{\text{VSMOW}}$  is the relative composition of the VSMOW (Vienna Standard Mean Ocean Water) standard.  $\delta^*$  represents the abundance of either  $^1\text{H}^2\text{H}^{16}\text{O}$  or  $^1\text{H}_2^{18}\text{O}$ . The second order parameter deuterium excess is defined by Dansgaard (1964) as  $\text{dex} = \delta\text{D} - 8\delta^{18}\text{O}$ .

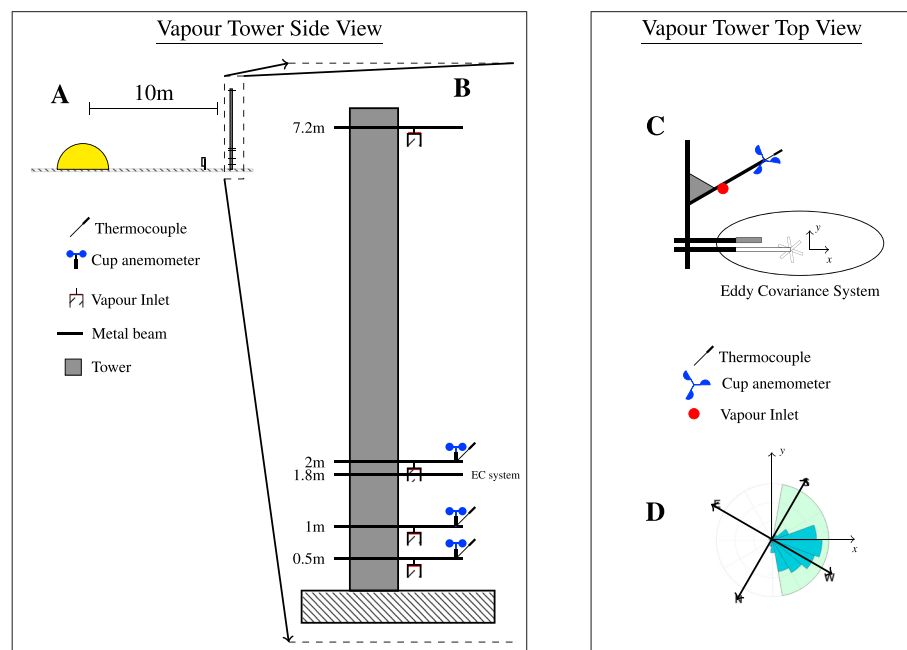


**Figure 1.** Schematic overview of the field site and instrument configuration. Side view: (a) Position of the tent, CR3000 micrologger, and vapor tower. The prevailing wind is approximately from right to left (see d). Vertical discretization of the model domain representation the lower boundary in contact with the snow surface. (b) Approximate position of vapor inlets, cup anemometers, fine-wire thermocouples, and the eddy covariance system. Top view: (c) Relative position of vapor inlets, cup anemometers, thermocouples, and eddy covariance instruments on each beam. A KH20 hygrometer and CSAT3 ultrasonic anemometer comprise the eddy covariance system. Note that instruments are not drawn to scale. The  $x$ - $y$  coordinate system is the internal coordinate system of the ultrasonic anemometer. (d) The wind rose observed by the ultrasonic anemometer (10-min averages) where directions are given both with respect to the orientation of the anemometer ( $x$ - $y$  coordinate system) and the approximate north-south compass (N-S, E-W). The green wedge indicates the angles within  $80^\circ$  of the  $x$  axis of the CSAT3.

Calibration of the CRDS data was performed following the protocol outlined in Steen-Larsen et al. (2013). Humidity-isotope calibrations were conducted 4 times throughout the field season to correct for humidity-induced bias. VSMOW-SLAP calibrations were carried out 6 times during the field campaign using three standards ( $\delta^{18}\text{O}$ : 0.4‰, -33.56‰, -54.05‰;  $\delta\text{D}$ : 2.8‰, -257.6‰, -424.1‰). The uncertainties are assumed to be equivalent to the uncertainties estimated by Steen-Larsen et al. (2014), which are for  $\delta^{18}\text{O}$  and  $\delta\text{D}$  are 0.23‰ and 1.4‰, respectively. Propagation of errors gives an uncertainty on the vapor dxs of 2.3‰. The humidity-mixing ratio measured by the spectrometer was calibrated using the humidity measurements from the nearby AWS.

Throughout the field season, snow samples were routinely collected for isotopic analysis. Along a 1-km marked transect, 26 samples of the upper 1 cm of snow were collected on a daily basis. These samples have been analyzed on a Picarro L-2130-i CRDS and calibrated to the VSMOW-SLAP scale using four standards ( $\delta^{18}\text{O}$ : -19.8‰, -33.8‰, -42.39‰, -50.12‰;  $\delta\text{D}$ : -152.93‰, -266.7‰, -341.24‰, -392.0‰) at the Alfred-Wegener-Institute, Bremerhaven. In this study, only the average value and standard deviation of these 26 samples for each day are shown. These values will be referred to as the observed snow isotopic composition with standard deviation  $\sigma_{\text{snow}}$ .

### 2.3. Atmospheric Eddy Covariance Measurements

To estimate the atmospheric flux of water vapor at EastGRIP, an eddy covariance system (hereafter EC) was mounted on the tower, 1.8 m above the snow surface (Figure 1). The EC system consisted of a fast response krypton hygrometer (KH20) and a highly sensitive omnidirectional ultrasonic anemometer (CSAT3), both produced by Campbell Scientific Inc. With this setup, we calculated the turbulent fluxes of momentum, heat, and moisture between the surface and atmosphere (Box & Steffen, 2001; Cullen et al., 2007; Forrer & Rotach, 1997). Stably stratified conditions prevail at EastGRIP, strong and persistent katabatic winds are expected to maintain shear-driven instabilities and reduce intermittency, allowing reliable calculation of turbulent fluxes from the eddy covariance statistics.

The raw data were sampled at 20 Hz and relayed to a micrologger (Campbell Scientific Inc. CR3000) placed approximately 1.5 m downwind from the tower (Figure 1). For the turbulent flux calculation, raw covariances were averaged over 10-min intervals. Three cup-anemometers and fine-wire thermocouples were also mounted at heights 0.54, 1.05, and 2.07 m above the snow surface. These instruments have been included in Figure 1 for completeness, but the associated time series are not discussed in this paper.

#### 2.3.1. Calibration

We correct for errors in our turbulent flux measurements following Cullen et al. (2007). Outliers are excluded iteratively using criteria adopted from Hojstrup (1993). Errors induced by wind deflection around nearby structures have been corrected by excluding all measurements taken at times when the wind is directed from the camp toward the mounted sensors. By only retaining winds with an incident angle of  $\pm 80^\circ$  relative to the  $x$  axis of the anemometer (Figure 1d), all potentially corrupted data have been discarded.

Errors associated with the anemometer tilt (Hyson et al., 1977; Tanner & Thurtell, 1969) and frequency response loss (Moncrieff et al., 1997; Moore, 1986) have been corrected. Tilt corrections are required to prevent cross contamination of velocities by small misalignment of the sensors. On average, tilt corrections change the sensible and latent heat flux by 0.4% and -0.3%, respectively. Spectral corrections are required to account for band-pass filtering due to the separation and limited frequency response of the instruments. The CSAT3 and KH20 sensors were mounted 20 cm apart. The internal path lengths of the CSAT3 and the KH20 sensors were set to 11.5 and 1 cm, respectively. Average flux increases of 0.8% and 13% for the sensible and latent heat flux have been obtained, respectively.

### 2.4. Observations of Water Vapor

We focus now on two periods with distinct diurnal cycles in the atmospheric state: 25–29 June (day of year [DOY] 177–181) and 21–25 July (DOY 203–207). These periods were chosen based on the criteria that we wanted at least four clear diurnal cycles with minimal change in mean synoptic conditions and mostly clear sky conditions all the time. Diurnal cycles are observed on other days but were not chosen as they did not fulfill the requirements. During the June period, weak atmospheric instability is observed from 12:00–18:00 UTC, whereas neutral stability is observed during these hours in the July period. Measurement of the eddy momentum and heat flux by the EC system allows for the calculation of the

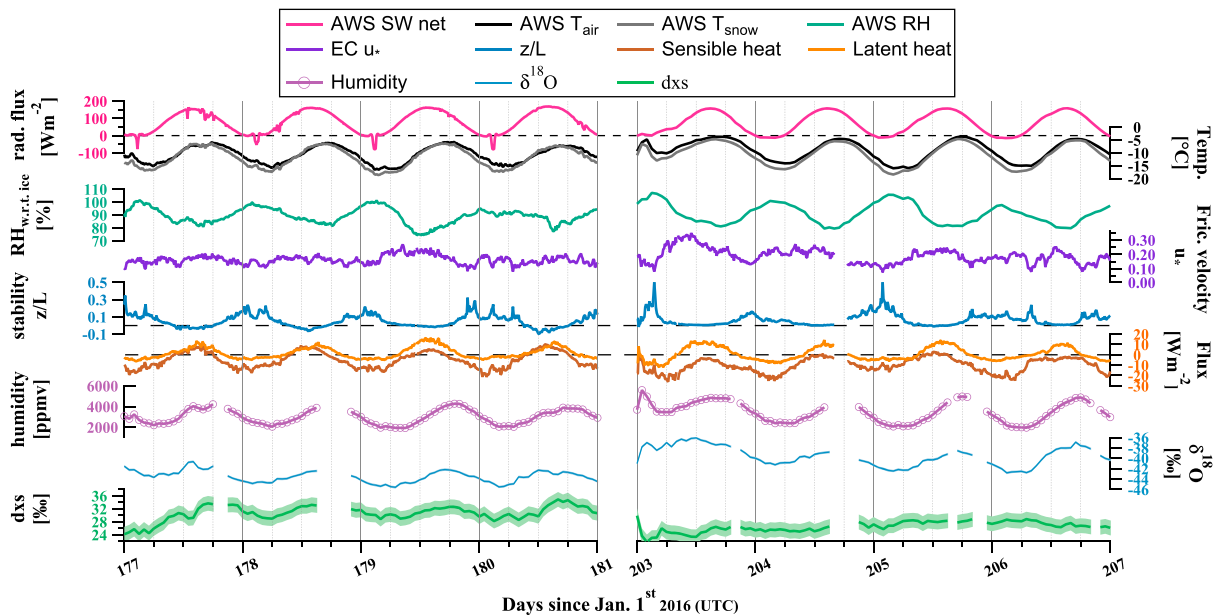


**Figure 2.** (left) June period (DOY 177–181, 25–29 June). (right) July period (DOY 203–207, 21–25 July). From above: Program for Monitoring of the Greenland Ice Sheet automatic weather station (AWS) observations of net incoming shortwave (SW) radiation, air and snow surface temperature, and relative humidity (RH) with respect to ice. Eddy Covariance observations of friction velocity, atmospheric stability ( $z/L$ ) evaluated at a height of 1.8 m, and turbulent sensible and latent heat flux. Specific humidity,  $\delta^{18}\text{O}$ , and  $dxs$  measured by the CRDS at 2 m above the snow surface. The shading on both  $\delta^{18}\text{O}$  and  $dxs$  indicates one measurement uncertainty. DOY = day of year.

friction velocity  $u^*$  and the Monin-Obukhov length,  $L$ , where  $L$  is proportional to the height at which buoyancy forcing dominates mechanical production of turbulence. The nondimensional stability parameter is defined as  $\zeta = z/L$ , where  $z$  is the height above the surface. Time series of  $\zeta$  and  $u^*$  are shown in Figure 2.

Although both June and July periods exhibit similar variation in atmospheric humidity, there are notable differences in observed vapor isotopic composition. Values of  $dxs$  throughout the June period show diurnal variations but are relatively constant during the July period. Furthermore, time-averaged  $dxs$  is larger in the earlier period. For reference, we note that in the June period, the time-averaged  $\delta^{18}\text{O}$  and  $\delta D$  is  $-43.5\text{‰}$  and  $-317.5\text{‰}$ , respectively, compared to July values of  $-39.6\text{‰}$  and  $-290.5\text{‰}$ . Supporting information S2 gives an overview of the water isotope observations from all four inlets for both the June and July period.

We shortly discuss relationships between the eddy covariance, humidity, and isotope observations. Typically, high (positive) stability is associated with a stable stratified lower atmosphere, where the snow surface is colder than the air above. This condition gives rise to a negative (downward) latent heat flux in the form of deposition or condensation causing the atmosphere to become less humid and more isotopic depleted. Further, in stable conditions little vertical mixing would occur and we would expect a gradient in both humidity and isotopic composition in the vapor (supporting information S2), where the vapor closest to the surface is more depleted and less humid than the air above. Opposite, unstable or near-neutral conditions result in an upward transport, positive heat fluxes and increasing humidity, and a uniform humidity and isotopic composition of the lower atmosphere (supporting information S2). We therefore expect, as also observed, a phase shift between the latent heat flux and the isotope observations since a positive latent heat flux infers sublimation from the surface, and the maximum humidity will occur at the time where the latent heat flux shifts from positive to negative.

### 3. Model

In this section, we construct a model to explore the observed variation of humidity,  $q(z,t)$ , and the vapor isotopic composition of  $\delta^{18}\text{O}(z,t)$  and  $\delta D(z,t)$ , with respect to time ( $t$ ) and displacement from the surface ( $z$ ). We aim to simulate the two periods with distinct  $dxs$  variations presented in section 2.4. The periods

will be referred to as the June and July periods, respectively. Both periods were cloud-free and characterized by repeating diurnal cycles of latent and sensible fluxes of heat, near-surface temperature, and humidity (Figure 2). The aim is to model the snow surface isotopic composition consistent with our humidity and isotope observations for these two cases.

The model consists of three boxes representing (1) the immediate snow surface, (2) a viscous sublayer (VSL), and (3) the near-surface ABL (Craig & Gordon, 1965).

The VSL has thickness  $\Delta z$  and is characterized by mixing dominated by molecular diffusion. At all times, it is assumed that the lower boundary of the VSL is saturated with respect to ice at the snow surface temperature  $T_s$ .

The model domain simulating the near-surface ABL extends from the top of the VSL to the height  $z = H$  and is characterized by turbulent mixing and no isotopic fractionation. This mixing rate is assumed to be the same for all isotopologues of water, in contrast to the molecular diffusion in the VSL, which is modeled with an isotopologue-dependent molecular diffusion. We set  $H = 7.2$  m, corresponding to the top inlet on the tower.

### 3.1. Numerical Formulation

We model the humidity and vapor isotopic composition with a diffusion equation

$$\frac{\partial R^* q}{\partial t} = \frac{\partial}{\partial z} \left( \kappa^*(z, t) \frac{\partial R^* q}{\partial z} \right) \quad (1)$$

where  $R^*$  is the ratio of the concentration of the rare isotopic species to the abundant  $^1\text{H}_2^{16}\text{O}$  and  $q$  is the mixing ratio.  $\kappa^*$  is the isotopologue-specific diffusion coefficient. To provide higher resolution near the surface where we expect the largest vertical gradients of  $q(z)$ ,  $\delta^{18}\text{O}(z)$ , and  $\delta\text{D}(z)$ , we introduce a vertically stretched coordinate system (Figure 1). The height  $z$  of a grid point given by  $z(s) = H [\exp(as) - 1] / [\exp(a) - 1]$ , where  $s$  is a normalized coordinate used to transform a linearly spaced coordinate system into the stretched coordinate. We set  $a = 8.2$ , generating 200 grid nodes that allow for reasonable computation times. Stable solutions to equation (1) are achieved using a Crank-Nicholson discretization scheme, with a time step of 2 min. Our discretization is independent of the VSL thickness  $\Delta z$ , which allows us to explore solutions to equation (1) under a broad range of  $\Delta z$ , without compromising numerical stability or increasing the computational cost of the model.

### 3.2. Diffusion Coefficient

We use the formulation of eddy diffusivity for momentum and heat inspired by Brost and Wyngaard (1978), and assume that the eddy diffusivity for sensible heat equals that of latent heat (Box & Steffen, 2001; Moore, 1986). In the near-surface ABL, we parameterize the turbulent diffusion coefficient,  $K_H(z, t)$ , as

$$K_H(z, t) = \frac{ku^* z' \left(1 - \frac{z'}{h}\right)^{1.5}}{\phi_m \left(\frac{z}{L}\right) \phi_H \left(\frac{z}{L}\right)} \quad (2)$$

Here,  $z$  is the height above the snow surface and  $z' = z - \Delta z$  is the height over the VSL. The distinction between  $z'$  and  $z$  is set so that  $K_H(z = \Delta z) = 0$ ;  $u^*$  the friction velocity and the von Karmán constant  $k = 0.4$ . We use the nondimensional functions  $\phi_m$  and  $\phi_H$  for momentum and heat (Högström, 1988) for both stable and unstable stratifications;  $h$  is the total height of the ABL, and we assume  $h > H$ . In this work, we use  $h$  as a free parameter to minimize the misfit between the observations and the model. The time dependency of  $K_H$  is contained in  $u^*$  and  $L$ , which are both derived directly from the eddy covariance measurements. The full diffusion coefficient is

$$\kappa^*(z, t) = \begin{cases} D^*(T_s, p) & \text{if } 0 \leq z \leq \Delta z \\ D^{16\text{O}}(T_s, p) + K_H(z, t) & \text{if } \Delta z < z \leq H \end{cases} \quad (3)$$

where  $D^*(T_s, p)$  is the isotopologue-specific molecular diffusion,  $T_s$  is the snow surface temperature, and  $p$  is the ambient atmospheric pressure. We use the molecular diffusivity of water vapor in air given by

Hall and Pruppacher (1976). The isotopologue-specific diffusivities in the VSL are given by the ratios  $D^{18\text{O}}/D^{16\text{O}} = 0.9723$  and  $D^{\text{D}}/D^{16\text{O}} = 0.9755$  (Merlivat, 1978).

### 3.3. Modeling Humidity

When modeling the humidity, we solve equation (1), with  $R^* = R^{16\text{O}} = 1$ . At the snow-VSL interface we force the model with the AWS observed radiative snow surface temperature and assume saturation with respect to ice. The saturation vapor pressure over ice is calculated following Flatau et al. (1992). The upper boundary of the model is forced with the observed humidity-mixing ratio obtained from the CRDS measurements. The model is initialized with a constant humidity throughout the box, prescribed as the saturation humidity at the snow surface temperature. We use a spin-up of 1 day. This means that to model for example the June period (26–29 June) we use 1-day integration forced by CRDS, EC, and AWS data from 25 June as spin-up.

### 3.4. Modeling Isotopic Composition of Water Vapor

We solved equation (1) for  $R^{18\text{O}}q$  and  $R^{\text{D}}q$  and initialized the simulations with uniform isotopic composition. The initialization values based on observational means were  $\delta^{18\text{O}} = -45\text{‰}$  and  $\delta\text{D} = -320\text{‰}$ . Similar to the humidity simulations, a 1-day spin-up is used. We force the upper boundary at  $z = H$  with the observed isotopic composition,  $R^{18\text{O}}q$  and  $R^{\text{D}}q$ . We do not have any measurements of the vapor isotopic composition at  $z = 0$ . Instead, we assume that the vapor isotopic composition at the snow-vapor interface varies diurnally (see Figure 2) following:

$$\delta^*(z = 0, t) = A^* + B^* \sin\left(\frac{2\pi t}{T_{\text{day}}} + C^*\right) \quad (4)$$

where  $T_{\text{day}} = 24$  hr,  $A^*$  is the mean isotopic composition,  $B^*$  is the amplitude, and  $C^*$  is the phase offset, for each isotopologue.  $A^*$ ,  $B^*$ , and  $C^*$  are unknown model parameters for each isotopologue.

We use a least squares optimization approach to minimize the total model-data misfit. The model parameters we seek to optimize are  $A^*$ ,  $B^*$ , and  $C^*$  in equation (4), along with the VSL thickness,  $\Delta z$ , and the ABL height,  $h$ . To compute the isotopologue misfit, the modeled isotopic composition is linearly interpolated onto the height of the three inlets on the tower at  $z = [0.56, 1.06, 2.07]$  m.

We have computed best fit values of  $A^*$ ,  $B^*$ , and  $C^*$ , referred to as  $A^*_{\text{best}}$ ,  $B^*_{\text{best}}$ , and  $C^*_{\text{best}}$ , respectively, for three different boundary layer heights  $h = [25, 75, 150]$  m and VSL thicknesses in the range  $0.0005 \text{ m} \leq \Delta z \leq 0.1 \text{ m}$ . Values for  $A^*$  and  $B^*$  have been run with a resolution of  $0.1\text{‰}$  and  $0.5\text{‰}$  for  $\delta^{18\text{O}}$  and  $\delta\text{D}$ , and the phase offset,  $C^*$  with a resolution of 30 min. No a priori constraints have been placed on the values of  $A^*$  and  $B^*$ .

## 4. Results and Discussion

Figure 3 shows values of  $A^*_{\text{best}}$ ,  $B^*_{\text{best}}$ , and  $C^*_{\text{best}}$  as a function of the VSL thickness  $\Delta z$ , and boundary layer height,  $h$ . In general, we find that the value of  $C^*_{\text{best}}$  for  $\delta^{18\text{O}}$  and  $\delta\text{D}$  is nearly independent of  $\Delta z$  and  $h$  during both the June and July period.  $A^*_{\text{best}}$  and  $B^*_{\text{best}}$  are almost independent of  $h$ , but vary approximately linearly with  $\Delta z$ . A positive linear relation between  $B^*_{\text{best}}$  and  $\Delta z$  is expected since the influence of the bottom boundary condition is more attenuated for a thicker VSL. For the rest of this study, we will only consider results from equation (4) using the optimized values of the three model coefficients  $A^*_{\text{best}}$ ,  $B^*_{\text{best}}$ , and  $C^*_{\text{best}}$  (Figure 3).

### 4.1. The June Period

The model-data misfits, calculated as described in section 3.4, of  $\delta^{18\text{O}}$ ,  $\delta\text{D}$ , and specific humidity,  $q$ , as a function of  $\Delta z$  are shown in Figure 4. The model-data misfit of  $q$  is shown at each of the three observed heights  $z = [0.5, 1, 2 \text{ m}]$ . For the investigated range of  $\Delta z$  and  $h$ , the model-data misfit in  $q$  is consistently smaller for the lowest level ( $z = 0.5 \text{ m}$ ). This misfit is strongly dependent on the choice of the VSL thickness,  $\Delta z$ , and weakly dependent on the ABL height,  $h$ . The optimal choice of  $\Delta z$ , depends on the height above the surface; the minimum misfit at heights  $z = [0.5, 1, 2] \text{ m}$  are found for a VSL thicknesses of  $\Delta z \sim [0.008, 0.006, 0.03] \text{ m}$ . At heights  $z = [0.5, 1, 2] \text{ m}$  the optimal combination of  $\Delta z$  and  $h$  has a [50%, 25%, 25%] reduction in model-data misfit, relative to the worst possible combination of  $\Delta z$  and  $h$  used in this study.

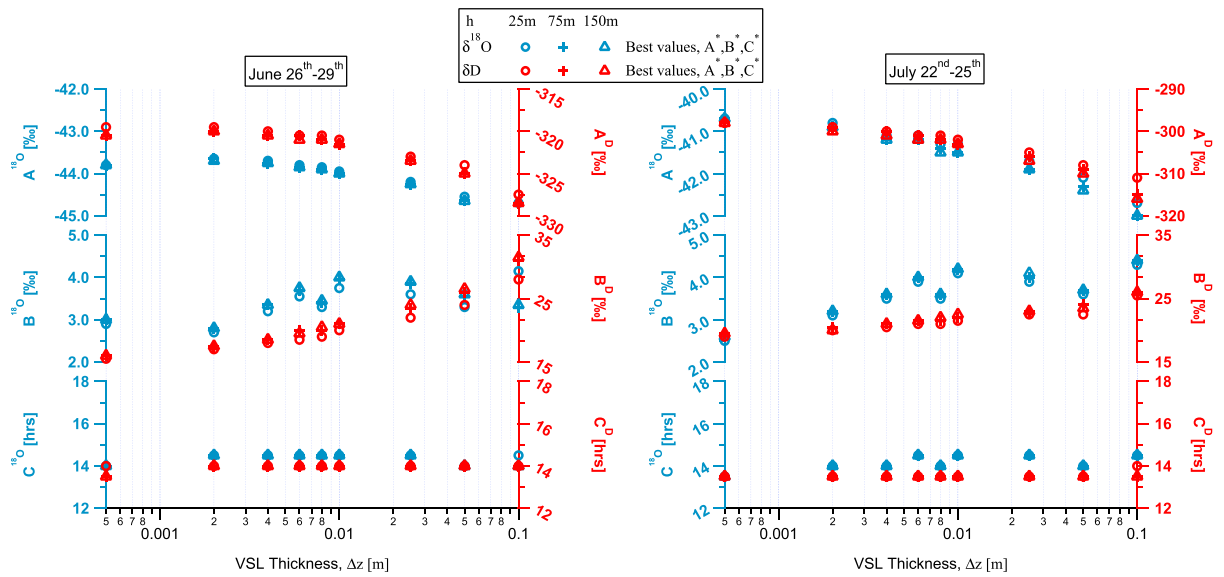


**Figure 3.** Values of the coefficients  $A^*$ ,  $B^*$ , and  $C^*$  in equation (4) for different combinations of viscous sublayer (VSL) thickness ( $\Delta z$ , x axis) and atmospheric boundary layer height ( $h$ , symbols—see key), shown for both (blue)  $\delta^{18}\text{O}$  and (red)  $\delta\text{D}$  producing the best fit to the observations. (left) June period. (right) July period.

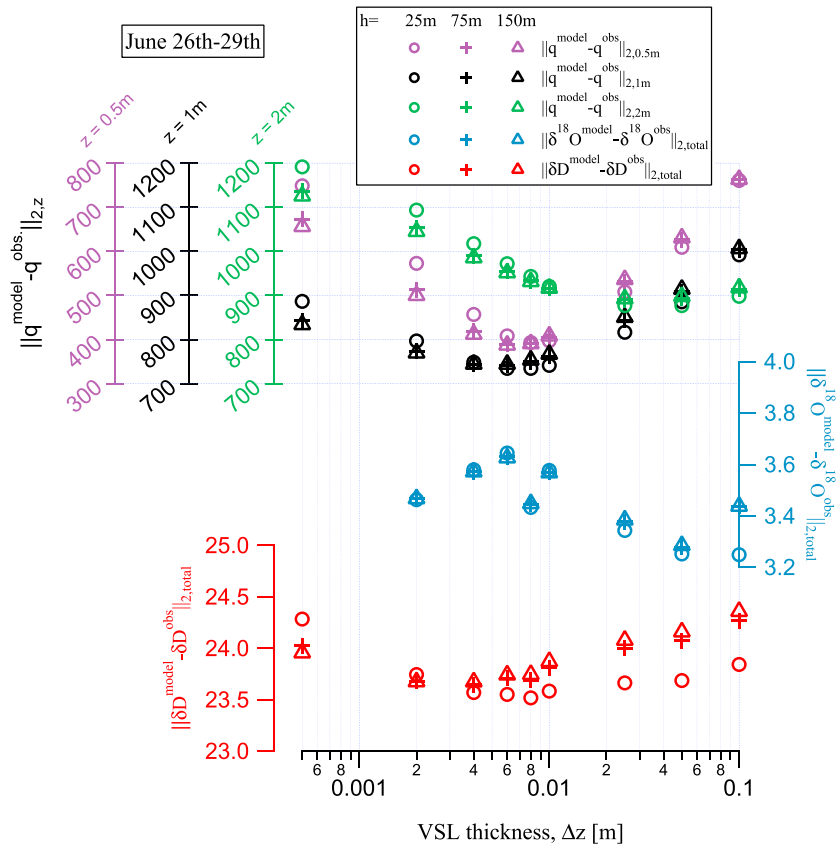


**Figure 4.** June period model-data misfit dependency on the thickness of the viscous sublayer (VSL)  $\Delta z$  for three different values of  $h$ : 25 (circles), 75 (crosses), and 150 m (triangles). (top) Humidity misfit for each individual level; the misfit at the 0.5-m level (purple) is consistently smaller than that at the 1- (black) and 2-m (green) levels. (middle) Total  $\delta^{18}\text{O}$  model-data misfit (blue). (bottom) Total model-data misfit for  $\delta\text{D}$  (red).

**Table 2**  
Best Fit Values for  $A^*$ ,  $B^*$ , and  $C^*$  for the June and July Period

Water vapor isotopic parameter	26–29 June			22–25 July		
	$A$ (‰)	$B$ (‰)	$C$ (hr)	$A$ (‰)	$B$ (‰)	$C$ (hr)
$\delta^{18}\text{O}$	−43.9	3.3 (1.7, 4.6)	14.5	−41.7	3.9(2.4, 4.6)	14.5
$\delta\text{D}$	−320.5	19.0 (10, 27.5)	14.0	−305.0	22.5(13.5, —)	13.5
$\text{dxs}$	31	−8	—	28	−11	—

*Note.* To achieve the overall best fit to both humidity and isotopic composition measurements, we find  $\Delta z = 0.008$  m and  $h_s = 25$  m for the June period, and  $\Delta z = 0.025$  m and  $h = 25$  m for the July period. The 95% confidence bound on  $B^*$  is given in the parentheses, an upper limit on  $B^{\text{D}}$  for the July period has not been determined (see supporting information S1).

Ideally, minimization of model-data misfits at the three levels should suggest the same optimal values of  $\Delta z$  and  $h$ . We find that the modeled humidity is slightly phase shifted relative to the observations at  $z = 2$  m on DOY 179. Furthermore, observed humidity at  $z = 1$  m on DOY 180 exhibits more noise relative to DOY 178 and 179, which cannot be reproduced by the model. As a result, larger model-data misfits are found at the  $z = [1, 2]$  m levels, relative to the  $z = 0.5$  m level (supporting information S3 and Figures S7–S9).

Despite these issues, our idealized model reproduces a significant fraction of the observed variability. Specifically, we are able to simulate 90–95% of the observed variance in  $q$  (i.e., modeled  $q$  variations are within 1 measurement uncertainty of the observations), by assuming a VSL thickness in the range  $0.006$  m  $< \Delta z < 0.01$  m, independent of the ABL height.

The model-data misfit in  $\delta^{18}\text{O}$  is maximized for a VSL thickness of  $\Delta z = 0.006$  m and minimized for thicknesses in the range  $0.05$  m  $< \Delta z < 0.1$  m. The model-data misfit in  $\delta\text{D}$  is minimized for a VSL thickness in the range  $0.004$  m  $< \Delta z < 0.008$  m. For both  $\delta^{18}\text{O}$  and  $\delta\text{D}$ , the optimal choice of  $\Delta z$  depends on the assumed ABL height,  $h$ . We find that the total model-data misfit for  $\delta^{18}\text{O}$  and  $\delta\text{D}$  can be reduced by 9% and 3% given the choice of  $\Delta z$  and  $h$ , respectively.

We select  $\Delta z = 0.008$  m and  $h = 25$  m to minimize the total model-data misfit for the June period. The values of  $A^*_{\text{best}}$ ,  $B^*_{\text{best}}$ , and  $C^*_{\text{best}}$  for the June period are shown in Table 2. See supporting information S3 for a comparison between model and observations with these settings.

#### 4.2. The July Period

We now focus on optimization of the model for the July period (DOY 204 to 207). Both humidity and the isotopologues dependence of model-data misfit on the VSL thickness  $\Delta z$ , and ABL height,  $h$ , are shown in Figure 5.

We find that the humidity model-data misfit is minimized for  $0.025$  m  $< \Delta z < 0.05$  m; as mentioned above, the optimal choice depends on the height above the surface. However, in contrast to the June period, we find that the worst model-data misfit in July is obtained for the lowest level ( $z = 0.5$  m; supporting information S3 and Figures S10–S12).

We observe trends for the total model-data misfit for  $\delta^{18}\text{O}$  and  $\delta\text{D}$  that are similar to those during the June period. Surprisingly, we note that the misfits for the two isotopes behave independently of the fit to the overall humidity, that is, that the minimum of the humidity is not aligned with the minimum in the total 2-norm of  $\delta\text{D}$ . The humidity misfit is also more drastically reduced due to the choice of  $\Delta z$  compared to the isotope misfits. Therefore, the best overall fit to the observations is obtained by settings  $\Delta z = 0.025$  m and  $h = 25$  m. The values of  $A^*_{\text{best}}$ ,  $B^*_{\text{best}}$ , and  $C^*_{\text{best}}$  using these settings are shown in Table 2. We refer to supporting information S3 for a comparison between model and observations with these settings.

#### 4.3. Snow Isotopic Composition

The results in the previous sections allow us to estimate the diurnal changes in the snow isotopic composition during the June and July periods, consistent with the water vapor isotope observations. To calculate the snow surface snow isotopic composition we assume equilibrium fractionation at the interface between the snow surface and the VSL. Using the optimized parameters  $A^*_{\text{best}}$ ,  $B^*_{\text{best}}$ , and  $C^*_{\text{best}}$  (Table 2), we compute

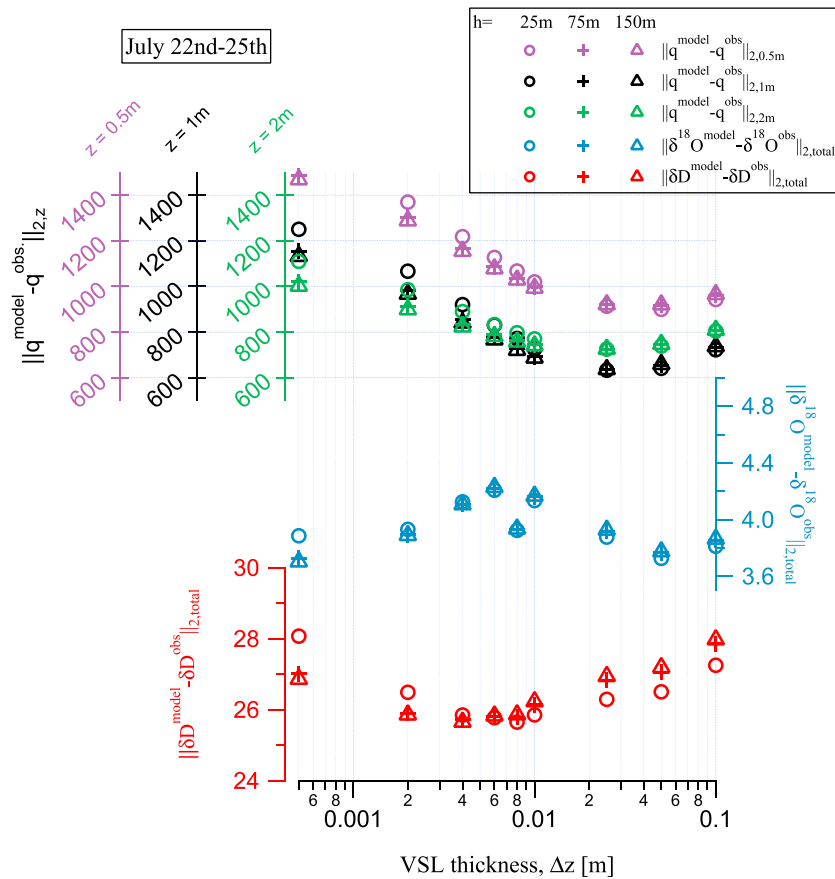


**Figure 5.** July period model-data misfit dependency on the thickness of the viscous sublayer (VSL)  $\Delta z$  for three different values of  $h$ : 25 (circles), 75 (crosses), and 150 m (triangles). (top) Humidity misfit for each individual level; the misfit at the 0.5-m level (purple) is consistently smaller than that at the 1- (black) and 2-m (green) levels. (middle) Total  $\delta^{18}O$  model-data misfit (blue). (bottom) Total model-data misfit for  $\delta D$  (red).

the snow isotopic composition using the fractionation coefficients  $\alpha$  for ice-vapor fractionation from Ellehoj et al. (2013) and the observed snow surface temperature. We note that using fractionation values from Majoube (1971) or Merlivat and Nief (1967) does not change our conclusions. We have computed the average and maximum amplitude of the snow isotopic composition and have propagated the 95% confidence limit of the vapor amplitudes into snow amplitudes. The model is compared with the observed snow isotopic composition at three times during both the June and July periods (Figure 6).

In Figure 6, we observe that the top 1 cm of the snow surface isotope measurements and the modeled snow isotopes are consistent with each other under the assumption of isotopic fractionation at the interface, but due to the low temporal sampling frequency of the snow samples, they are not directly comparable. Furthermore, it is important to note that it is still unresolved to which depth the atmospheric water vapor is in contact with the top of the snow pack. To verify or reject the hypothesis that the snow surface is in isotopic equilibrium with the vapor at the snow-air interface, the surface snow would have to be sampled in higher vertical and temporal resolution (millimeter and hourly, respectively). However, it is possible to model the depth to which the snow should be in isotopic equilibrium with the vapor.

We have estimated in Table 3b the depth of the snow surface that remains in equilibrium with the vapor at the lower boundary of the VSL by using the principle of conservation of isotopic composition and assuming isotopic fractionation. We do this using EC measurements of the latent heat flux, the fractionation coefficients given by Ellehoj et al. (2013), and the constants given in Table 3a. The required depth of the snow surface, which is in equilibrium with the vapor at the lower boundary of the VSL interphase, is computed for both the June and July period using the amplitudes and the confidence interval given in Table 2. As a

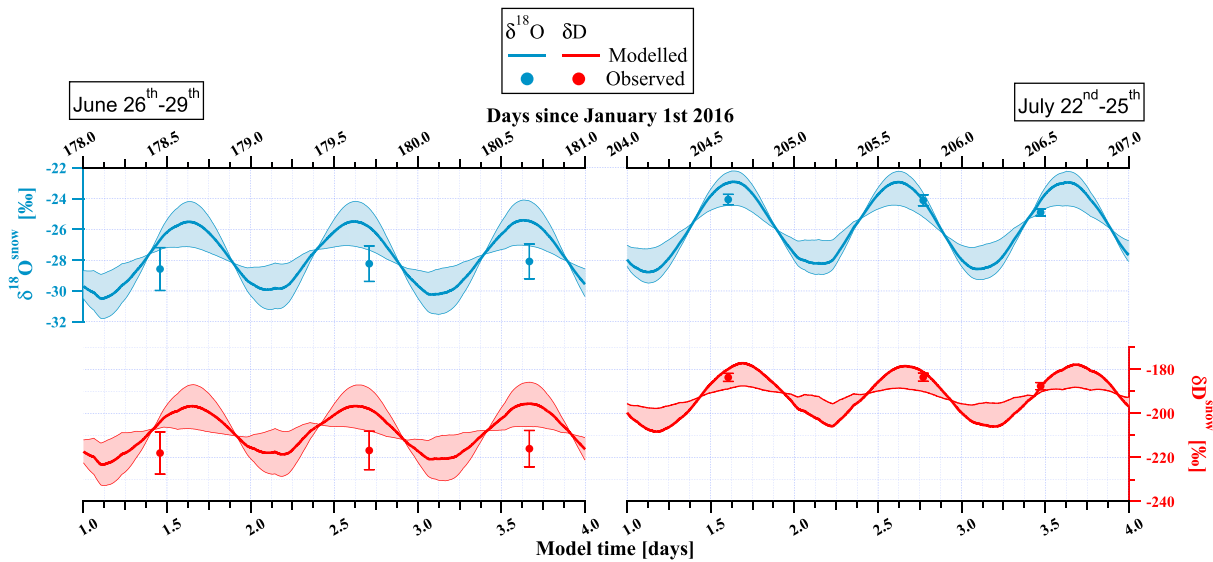


**Figure 6.** Snow isotopic composition using the ice-vapor fractionation coefficient from Ellehoj et al. (2013), assuming equilibrium fractionation in the viscous sub-layer. (left) June period. (right) July period. For each period, three observations of snow isotopic composition are also shown. The standard deviation ( $\sigma_{\text{snow}}$ ) on the mean observed snow isotopic composition is comparable to the marker size for the July period.

result of these calculations, we observe that within the uncertainty range of our tuned parameters, the snow depth of the layer in equilibrium with the vapor will be in the submillimeter to centimeter range (Table 3b).

In conclusion, our model simulates during summer cloud-free conditions at EastGRIP that the snow isotopic composition exhibits diurnal variations with an amplitude of around 2.5‰ and 13‰ for  $\delta^{18}\text{O}$  and  $\delta\text{D}$ , respectively. Such variations are significant as they are on the order of 10–20% of seasonal variations measured in snow pack isotopes (Shuman et al., 1998; Steen-Larsen et al., 2011). Similarly do the estimated diurnal changes in the snow isotopes also correspond to 10–20% of glacial-interglacial transitions in Greenland (e.g., Johnsen et al., 2001). It is possible that these large diurnal variations in isotopic composition may be limited to the upper few millimeters of the snow. Further work to model vapor diffusion within the snow pack could help determine the maximum depth at which the snow is influenced by these processes. Validation of our model results will require carefully conducted snow sampling in future field experiments.

We suggest that the simulated and observed snow isotopic compositions are evidence of fractionation during the diurnal vapor to ice and ice to vapor phase transitions. For the June period, this conclusion is based on the observation that the snow samples are consistent with the average value of the modeled snow isotopic composition within  $1\sigma_{\text{snow}}$  for both isotopic species when assuming isotopic fractionation at the interface between the air and the snow surface. This agreement is independent of the specific choice of fractionation coefficients from the available range published in the literature. For the July period, we observe an agreement within  $1\sigma_{\text{snow}}$  and the 95% confidence bound on the modeled snow isotopic

**Table 3a**  
Values Used for Estimating Snow Surface Thickness in Equilibrium With the Vapor in the Viscous Sublayer

	Symbol	Value
Latent heat of sublimation at 0 °C	$\lambda$	2838 kJ/kg
Snow density	$\rho_s$	150 kg/m <sup>3</sup>
Snow surface temperature	$T_s$	-11.5 °C
Average day positive latent heat flux (June/July)	$L_E > 0$	6.5/6.7 W/m <sup>2</sup>
Average day negative latent heat flux (June/July)	$L_E < 0$	-2.5/-3.8 W/m <sup>2</sup>
Initial snow surface isotopic composition	$\delta^{18}\text{O}$	-30‰
Initial snow surface isotopic composition	$\delta\text{D}$	-240‰

**Table 3b**

*Estimates of the Snow Thickness at Which the Snow Is in Equilibrium With the Vapor Above the Surface Given the State of the Latent Heat Flux (Positive or Negative)*

	Water vapor isotope parameter	June period (mm)	July period (mm)
$L_E > 0$	$\delta^{18}\text{O}$	2.5(7.1, 1.8)	2.3 (4.5, 1.9)
	$\delta\text{D}$	3.2(14.4, 1.9)	2.0 (9.9, —)
$L_E < 0$	$\delta^{18}\text{O}$	0.7 (2.5, 0.4)	0.9 (2.2, 0.7)
	$\delta\text{D}$	1.0 (5.3, 0.5)	1.2 (5.2, —)

*Note.* The 95% confidence bounds are giving in the parentheses.

composition. We conclude that accounting for isotopic fractionation is important in modeling snow-atmosphere isotopic exchange. This implies that the snow isotopic composition can change while the snow is subjected to exchange with the atmosphere.

Until this point we have not considered how the model performs in terms of dxs. In summary, given that we use the optimized values for  $A^*$ ,  $B^*$ , and  $C^*$ , we find that we are able to simulate the dxs such that on average 95% of the modeled dxs is within one standard deviation of the observed values.

However, the modeled dxs limits the maximum deviation of  $B^{18}\text{O}$  from  $B^{\text{D}}$ . For example, by selecting the upper bound of the confidence limit on  $\delta\text{D}$  and the lower bound on the confidence limit of  $\delta^{18}\text{O}$ , we find that

we no longer simulate the dxs within 95% confidence. This implies that an optimization of the parameters  $A^*$  and  $B^*$  with respect to dxs will result in a reduction of the confidence limits given in Table 2. Since a reduction in the confidence bounds on  $B^*$  does not undermine our results we find that another optimization of the parameters with respect to dxs is unnecessary. Nonetheless, it is important to note that we find that the modeled vapor at the snow-VSL interface have a diurnal cycle in the dxs for both the June and July period (Table 2). For both periods we find that the modelled vapor dxs is in antiphase with the  $\delta\text{D}$  and  $\delta^{18}\text{O}$  at the snow-VSL interface, even though there is no diurnal cycle in the atmospheric vapor for the July period. This is a result of the presences of the VSL, where the difference in molecular diffusivities determines how the dxs attenuates with displacement from the surface.

We now compare our results to existing studies. Ritter et al. (2016) find evidence in their snow samples of a diurnal cycle with amplitude  $\sim 0.2\text{‰}$  and  $\sim 1.5\text{‰}$  for  $\delta^{18}\text{O}$  and  $\delta\text{D}$ , respectively. This amplitude is smaller than our modeled amplitude, which in part can be explained by both lower temperatures and lower specific humidity, since the observations of Ritter et al. (2016) are conducted at Kohnen Station, Antarctica. To verify this, we have conducted sensitivity studies (not shown) and found that a 15–20% reduction in snow isotope amplitude is achieved for a cooling of 10 K, consistent with summer conditions at Kohnen Station. However, the most important factor is probably related to the difficulties of sampling the exact top of the snow pack layer. Steen-Larsen et al. (2014) present two summer seasons of snow samples collected from the top 0.5 cm. Their morning and evening samples indicate a diurnal cycle with maximum amplitudes of 0.6‰ for  $\delta^{18}\text{O}$ .

Isotopes have recently been implemented in the complex snowpack model CROCUS (Touzeau et al., 2018). The authors propose, similar to Ebner et al. (2017), that a snow grain has an inner and outer isotopic composition, which is similar upon snowfall, but changes independently as the snow grain undergoes postdepositional processes. We propose that throughout a single day, the outer snow grain undergoes substantial changes in both volume and isotopic composition, whereas the inner snow grain isotopic composition stays constant. This can partly explain the difference between the modeled and observed change observed in this work, since a snow sample would be biased toward inner grain isotopic composition, and thus, the observed diurnal variability in the surface snow isotopic composition would be damped.

It is unclear how this conclusion is compatible with Pinzer et al. (2012), who used controlled lab experiments with X-ray tomography to show that an average snow crystal has a lifetime of 2–3 days, with a daily mass turnover of up to 60%. Further studies are needed to address the interplay between changes in the snow isotopic composition caused by snow metamorphism and equilibration of the outer snow grain with the near-surface atmospheric water vapor.

## 5. Conclusions

We have presented near-continuous, high-precision measurements of water isotopic composition in atmospheric vapor, as well as eddy covariance measurements from two periods of stable diurnal cycles, taken at the EastGRIP camp during summer 2016. We observe substantial changes in the isotopic composition of the near-surface atmosphere on diurnal timescales, which prompted an investigation as to whether these high-frequency isotopic variations are also present in the surface snow. We focus on simulating two distinct cloud-free periods from the 2016 field season, spanning three days each. Although both periods exhibit

similar variation in atmospheric humidity, there are notable differences in observed vapor isotopic compositions.

We have developed a numerical model to simulate changes in humidity and water vapor isotopic composition along a vertical profile extending from the snow surface up into the near-surface atmosphere. With this model, we are able to compute the snow isotopic composition and quantify the amplitude of snow isotope variability across diurnal cycles. We find that the uppermost millimeters of the snow surface in northeast Greenland exhibits a diurnal variability with an amplitude of approximately 2.5‰ and 13‰ for  $\delta^{18}\text{O}$  and  $\delta\text{D}$ , respectively. The magnitude of these diurnal variations in the snow is significant and equivalent to 10–20% of the seasonal change in the snow isotopic composition in Greenland, or of the magnitude of the change across a glacial-interglacial transition.

We also compared our modeled snow isotopic composition with measurements of the integrated top 1 cm of snow. Based on the snow and vapor isotope measurements, we conclude that the observations are consistent with the assumption of isotopic equilibrium at the snow-air interface. Our findings highlight the need for a high-resolution sampling campaign in order to improve our understanding on the processes controlling isotopic fractionation of snow during sublimation. Our results strongly support the earlier findings that a diurnal signal exists in the snow isotopic composition. Further laboratory experiments and fieldwork can address the following questions: Does a viscous sublayer exist as an interface between the snow and the near-surface atmosphere? What is the thickness of the viscous sublayer? To what depth is diurnal variability in snow isotopic composition significant? It is needed to sample the uppermost millimeters of the snow at high frequency in both laboratory and field experiments to answer this question.

We have found evidence that fractionation during sublimation and solid-condensation is important for modeling vapor exchange and snow isotopic composition on the diurnal scale, supporting recently published results by Ritter et al. (2016). This implies that the snow isotopic composition can change while the snow is subjected to exchange with the atmosphere. This work therefore contributes to the understanding of how the isotopic composition of snow is subject to changes after deposition. The ability of the presented model to simulate the diurnal cycle in isotopic composition of the vapor and change in the snow isotopic composition yield confidence in the ability to further parameterize the snow-air interaction and eventually implement this into higher complexity climate models. This is relevant for both present-day and paleoclimate modeling of Greenland isotopes and comparison to ice core records.

#### Acknowledgments

EGRIP is directed and organized by the Center of Ice and Climate at the Niels Bohr Institute. It is supported by funding agencies and institutions in Denmark (A. P. Møller Foundation, University of Copenhagen), USA (U.S. National Science Foundation, Office of Polar Programs), Germany (Alfred Wegener Institute, Helmholtz Centre for Polar and Marine Research), Japan (National Institute of Polar Research and Arctic Challenge for Sustainability), Norway (University of Bergen and Bergen Research Foundation), Switzerland (Swiss National Science Foundation), France (French Polar Institute Paul-Emile Victor, Institute for Geosciences and Environmental research), and China (Chinese Academy of Sciences and Beijing Normal University). This project has received funding from the European Research Council (ERC) under the European Union's Horizon 2020 research and innovation program: Starting Grant-SNOWISO (grant agreement 759526). The authors acknowledge James DeGrand for calibrating the KH-20 instrument and updating the CSAT3D firmware. Data from the Program for Monitoring of the Greenland Ice Sheet (PROMICE) were provided by the Geological Survey of Denmark and Greenland (GEUS; <http://www.promice.dk>). M. V. M. thanks the Frederikke Lørup's mindelegat for support of visit to University of Colorado. AH acknowledges a Professorial Fellowship from CAGE funded through RCN grant 223259. Data are available as supporting information in ascii and excel format. Questions regarding data should be addressed to H. C. Steen-Larsen (hans.christian.steen-larsen@uib.no).

#### References

- Ahlstrøm, A., Gravesen, P., Andersen, S., As, D. V., Citterio, M., Fausto, R., et al. (2008). A new programme for monitoring the mass loss of the Greenland ice sheet. *Geological Survey of Denmark and Greenland Bulletin*, *15*, 61–64.
- Box, J. E., & Steffen, K. (2001). Sublimation on the Greenland Ice Sheet from automated weather station observations. *Journal of Geophysical Research*, *106*(33), 965–33,981. <https://doi.org/10.1029/2001JD900219>
- Brost, R. A., & Wyngaard, J. C. (1978). A model study of the stably stratified planetary boundary layer. *Journal of the Atmospheric Sciences*, *35*, 1427–1440. [https://doi.org/10.1175/1520-0469\(1978\)035<1427:amsots>2.0.co;2](https://doi.org/10.1175/1520-0469(1978)035<1427:amsots>2.0.co;2)
- Casado, M., Landais, A., Picard, G., Münch, T., Laepple, T., Stenni, B., et al. (2018). Archival processes of the water stable isotope signal in East Antarctic ice cores. *The Cryosphere*, *12*, 1745–1766. <https://doi.org/10.5194/tc-12-1745-2018>
- Craig, H. (1961). Isotopic variations in meteoric waters. *Science*, *133*, 1702–1703.
- Craig, H., & Gordon, L. I. (1965). Deuterium and oxygen 18 variations in the ocean and the marine atmosphere. In E. Tongiogi (Ed.), *Stable isotopes in oceanographic studies and paleotemperatures* (pp. 9–130). V. Lishi e F., Pisa, Spoleto, Italy.
- Cullen, N. J., Steffen, K., & Blanken, P. D. (2007). Nonstationarity of turbulent heat fluxes at Summit, Greenland. *Boundary-Layer Meteorology*, *122*, 439–455. <https://doi.org/10.1007/s10546-006-9112-2>
- Dansgaard, W. (1964). Stable isotopes in precipitation. *Tellus*, *16*, 436–468.
- Ebner, P. P., Steen-Larsen, H. C., Stenni, B., Schneebeli, M., & Steinfeld, A. (2017). Experimental observation of transient  $\delta^{18}\text{O}$  interaction between snow and advective airflow under various temperature gradient conditions. *The Cryosphere*, *11*, 1733–1743. <https://doi.org/10.5194/tc-11-1733-2017>
- Ellehoj, M. D., Steen-Larsen, H. C., Johnsen, S. J., & Madsen, M. B. (2013). Ice-vapor equilibrium fractionation factor of hydrogen and oxygen isotopes: Experimental investigations and implications for stable water isotope studies. *Rapid Communications in Mass Spectrometry*, *27*, 2149–2158. <https://doi.org/10.1002/rcm.6668>
- EPICA Community Members (2006). One-to-one coupling of glacial climate variability in Greenland and Antarctica. *Nature*, *444*, 195–198.
- Flatau, P. J., Walko, R. L., & Cotton, W. R. (1992). Polynomial fits to saturation vapor pressure. *Journal of Applied Meteorology*, *31*, 1507–1513.
- Forrer, J., & Rotach, M. W. (1997). On the turbulence structure in the stable boundary layer over the Greenland ice sheet. *Boundary-Layer Meteorology*, *85*, 111–136. <https://doi.org/10.1023/a:1000466827210>
- Hall, W. D., & Pruppacher, H. R. (1976). The survival of ice particles falling from cirrus clouds in subsaturated air. *Journal of Atmospheric Science*, *33*, 1995–2006.

- Högström, U. (1988). Non-dimensional wind and temperature profiles in the atmospheric surface layer: A re-evaluation. *Boundary-Layer Meteorology*, *42*, 55–78. <https://doi.org/10.1007/bf00119875>
- Hojstrup, J. (1993). A statistical data screening procedure. *Measurement Science and Technology*, *4*, 153.
- Hyson, P., Garratt, J. R., & Francey, R. J. (1977). Algebraic and electronic corrections of measured uw covariance in the lower atmosphere. *Journal of Applied Meteorology*, *16*, 43–47. [https://doi.org/10.1175/1520-0450\(1977\)016<0043:aaecom>2.0.co;2](https://doi.org/10.1175/1520-0450(1977)016<0043:aaecom>2.0.co;2)
- Johnsen, S. J., Dahl-Jensen, D., Gundestrup, N., Steffensen, J. P., Clausen, H. B., Miller, H., et al. (2001). Oxygen isotope and palaeotemperature records from six Greenland ice-core stations: Camp Century, Dye-3, GRIP, GISP2, Renland and NorthGRIP. *Journal of Quaternary Science*, *16*, 299–307.
- Johnsen, S. J., Dansgaard, W., & White, J. W. C. (1989). The origin of Arctic precipitation under present and glacial conditions. *Tellus B*, *41*, 452–468.
- Jouzel, J., Alley, R. B., Cuffey, K. M., Dansgaard, W., Grootes, P., Hoffmann, G., et al. (1997). Validity of the temperature reconstruction from water isotopes in ice cores. *Journal of Geophysical Research*, *102*(26), 471–26,487.
- Jouzel, J., Masson-Delmotte, V., Cattani, O., Dreyfus, G., Falourd, S., Hoffmann, G., et al. (2007). Orbital and millennial Antarctic climate variability over the past 800,000 years. *Science*, *317*, 793–796.
- Majoube, M. (1971). Fractionnement en oxygène 18 et en deutérium entre l'eau et sa vapeur. *Journal de Chimie Physique*, *68*, 1423–1436.
- Masson-Delmotte, V., Landais, A., Stievenard, M., Cattani, O., Falourd, S., Jouzel, J., et al. (2005). Holocene climatic changes in Greenland: Different deuterium excess signals at Greenland Ice Core Project (GRIP) and NorthGRIP. *Journal of Geophysical Research*, *110*, D14102. <https://doi.org/10.1029/12004JD005575>
- Masson-Delmotte, V., Steen-Larsen, H. C., Ortega, P., Swingedouw, D., Popp, T., Vinther, B. M., et al. (2015). Recent changes in north-west Greenland climate documented by NEEM shallow ice core data and simulations, and implications for past-temperature reconstructions. *The Cryosphere*, *9*, 1481–1504. <https://doi.org/10.5194/tc-9-1481-2015>
- Merlivat, L. (1978). Molecular Diffusivities of (H<sub>2</sub>O)-O-16, HD16O, and (H<sub>2</sub>O)-O-18 in Gases. *Journal of Chemical Physics*, *69*, 2864–2871.
- Merlivat, L., & Nief, G. (1967). Fractionnement isotopique lors des changements d'état solide-vapeur et liquide-vapeur de l'eau à des températures inférieures à 0 °C. *Tellus*, *1*, 122–127.
- Moncrieff, J. B., Monteny, B., Verhoef, A., Friborg, T., Elbers, J., Kabat, P., et al. (1997). Spatial and temporal variations in net carbon flux during HAPEX-Sahel. *Journal of Hydrology*, *188-189*, 563–588. [https://doi.org/10.1016/S0022-1694\(96\)03193-9](https://doi.org/10.1016/S0022-1694(96)03193-9)
- Moore, C. J. (1986). Frequency response corrections for eddy correlation systems. *Boundary-Layer Meteorology*, *37*, 17–35. <https://doi.org/10.1007/bf00122754>
- NEEM Community Members (2013). Eemian interglacial reconstructed from a Greenland folded ice core. *Nature*, *493*, 489–494. <https://doi.org/10.1038/nature11789>
- North Greenland Ice-Core Project Members (2004). High resolution climate record of the Northern Hemisphere reaching into the last Glacial Interglacial Period. *Nature*, *431*, 147–151.
- Pinzer, B. R., Schneebeli, M., & Kaempfer, T. U. (2012). Vapor flux and recrystallization during dry snow metamorphism under a steady temperature gradient as observed by time-lapse micro-tomography. *The Cryosphere*, *6*, 1141–1155. <https://doi.org/10.5194/tc-6-1141-2012>
- Risi, C., Bony, S., Vimeux, F., & Jouzel, J. (2010). Water stable isotopes in the LMDZ4 General Circulation Model: model evaluation for present day and past climates and applications to climatic interpretations of tropical isotopic records. *Journal of Geophysical Research*, *115*, D12118. <https://doi.org/10.1029/2009JD013255>
- Ritter, F., Steen-Larsen, H. C., Werner, M., Masson-Delmotte, V., Orsi, A., Behrens, M., et al. (2016). Isotopic exchange on the diurnal scale between near-surface snow and lower atmospheric water vapor at Kohnen station, East Antarctica. *The Cryosphere Discussions*, *2016*, 1–35. <https://doi.org/10.5194/tc-2016-4>
- Shuman, C. A., Alley, R. B., Fahnestock, M. A., Bindschadler, R. A., White, J. W. C., Winterle, J., & McConnell, J. R. (1998). Temperature history and accumulation timing for the snowpack at GISP2, central Greenland. *Journal of Glaciology*, *44*, 21–30.
- Steen-Larsen, H. C., Johnsen, S. J., Masson-Delmotte, V., Stenni, B., Risi, C., Sodemann, H., et al. (2013). Continuous monitoring of summer surface water vapor isotopic composition above the Greenland Ice Sheet. *Atmospheric Chemistry and Physics*, *13*, 4815–4828. <https://doi.org/10.5194/acp-13-4815-2013>
- Steen-Larsen, H. C., Masson-Delmotte, V., Hirabayashi, M., Winkler, R., Satow, K., Prié, F., et al. (2014). What controls the isotopic composition of Greenland surface snow? *Climate of the Past*, *10*, 377–392. <https://doi.org/10.5194/cp-10-377-2014>
- Steen-Larsen, H. C., Masson-Delmotte, V., Sjolte, J., Johnsen, S. J., Vinther, B. M., Breon, F. M., et al. (2011). Understanding the climatic signal in the water stable isotope records from the NEEM shallow firn/ice cores in northwest Greenland. *Journal of Geophysical Research*, *116*, D06108. <https://doi.org/10.1029/2010JD014311>
- Tanner, C. B., & Thurtell, G. W. (1969). Anemoclinometer measurements of Reynolds stress and heat transport in then atmospheric surface layer, University of Wisconsin Tech. Rep. ECOM-66-G22-F, 8 8 pp.
- Touzeau, A., Landais, A., Morin, S., Arnaud, L., & Picard, G. (2018). Numerical experiments on vapor diffusion in polar snow and firn and its impact on isotopes using the multi-layer energy balance model Crocus in SURFEX v8.0. *Geoscientific Model Development*, *11*, 2393–2418. <https://doi.org/10.5194/gmd-11-2393-2018>
- Uemura, R., Masson-Delmotte, V., Jouzel, J., Landais, A., Motoyama, H., & Stenni, B. (2012). Ranges of moisture-source temperature estimated from Antarctic ice cores stable isotope records over glacial-interglacial cycles. *Climate of the Past*, *8*, 1109–1125. <https://doi.org/10.5194/cp-8-1109-2012>
- Vimeux, F., Masson, V., Jouzel, J., Stievenard, M., & Petit, J. R. (1999). Glacial-interglacial changes in ocean surface conditions in the Southern Hemisphere. *Nature*, *398*, 410–413.
- Vinther, B. M., Jones, P. D., Briffa, K. R., Clausen, H. B., Andersen, K. K., Dahl-Jensen, D., & Johnsen, S. J. (2010). Climatic signals in multiple highly resolved stable isotope records from Greenland. *Quaternary Science Reviews*, *29*, 522–538.
- Werner, M., Langebroek, P. M., Carlsen, T., Herold, M., & Lohmann, G. (2011). Stable water isotopes in the ECHAM5 general circulation model: Toward high-resolution isotope modeling on a global scale. *Journal of Geophysical Research*, *116*, D15109. <https://doi.org/10.1029/2011JD015681>
- Wong, T. E., Nusbaumer, J., & Noone, D. C. (2017). Evaluation of modeled land-atmosphere exchanges with a comprehensive water isotope fractionation scheme in version 4 of the Community Land Model. *Journal of Advances in Modeling Earth Systems*, *9*, 978–1001. <https://doi.org/10.1002/2016MS000842>